
Stronger ViTs With Octic Equivariance

David Nordström¹, Johan Edstedt², Fredrik Kahl¹, Georg Bökman¹

¹Chalmers University of Technology ²Linköping University

davnords@chalmers.se, johan.edstedt@liu.se,
fredrik.kahl@chalmers.se, bokman@chalmers.se

Codes and models: <https://github.com/davnords/octic-vits>

Abstract

Recent efforts at scaling computer vision models have established Vision Transformers (ViTs) as the leading architecture. ViTs incorporate weight sharing over image patches as an important inductive bias. In this work, we show that ViTs benefit from incorporating equivariance under the octic group, i.e., reflections and 90-degree rotations, as a further inductive bias. We develop new architectures, octic ViTs, that use octic-equivariant layers and put them to the test on both supervised and self-supervised learning. Through extensive experiments on DeiT-III and DINOv2 training on ImageNet-1K, we show that octic ViTs yield more computationally efficient networks while also improving performance. In particular, we achieve approximately 40% reduction in FLOPs for ViT-H while simultaneously improving both classification and segmentation results.

1 Introduction

In the pursuit of flexible yet scalable models, Vision Transformers (ViTs) [21] have emerged as the dominant architecture in modern computer vision. Key to their success is the combination of visual tokens, constructed from image patches, with the powerful attention mechanism [48], resulting in an extremely versatile yet scalable architecture. This scalability is due in large part to weight-sharing between the tokens, which ensures permutation *equivariance*.

Equivariance provides a powerful inductive bias in neural networks by enforcing structured responses to transformations such as translations, rotations or reflections. Another major benefit of equivariance is the reduction in computational cost from weight-sharing due to equivariance constraints. It is therefore interesting to investigate whether imbuing models with further equivariance yields stronger performance and better scaling. To this end, equivariance to roto-reflections, formalized through the octic group D_8 , is a particularly attractive group, as many vision tasks exhibit such symmetries, making it a natural inductive bias.

D_8 equivariance was introduced to convolutional networks by Cohen and Welling [13], demonstrating improved parameter efficiency by constraining the learnable space through group structure [55, 3, 52]. Yet, despite its theoretical appeal, state-of-the-art vision models [39, 37, 31, 51] do not incorporate such structure. We argue that this is not due to a lack of utility, but to practical limitations: most existing implementations construct equivariant layers using computationally inefficient architectures, leading to increased FLOPs and runtime. Without efficient, hardware-compatible implementations, these methods have remained impractical for large-scale models. As a result, the potential of equivariant design remains largely unexplored in state-of-the-art systems, in particular in the context of ViTs. Recently, Bökman et al. [8] showed that equipping ViTs with horizontal flip equivariance results in retained performance while saving FLOPs. However, their improvements are limited due to the small cardinality of their chosen group.

In this paper, we demonstrate that scaling equivariance to larger groups can be efficiently implemented – yielding faster, stronger, and more compact models, cf. Figure 1. Specifically, we introduce octic-

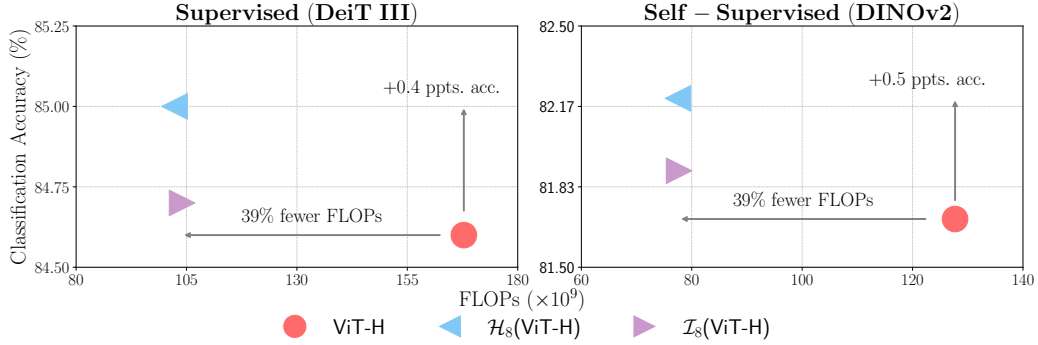


Figure 1: **Computational savings.** Using octic layers in ViTs significantly reduces the computational complexity while maintaining or improving classification accuracy on ImageNet-1K, for both supervised and self-supervised training. Detailed results can be found in Section 4.

equivariant layers for ViTs, leveraging the D_8 symmetry group of 90° rotations and reflections, cf. Figure 2. Our approach integrates seamlessly into existing ViT architectures and leads to significant gains in throughput and memory efficiency, without sacrificing accuracy.

In summary, our contributions are as follows:

- (a) We introduce octic-equivariant layers for ViTs, described in Section 3, that, when incorporated, achieve substantially higher FLOP efficiency given their representational capacity.
- (b) We develop an efficient implementation, including a custom Triton kernel for the activation function, to enable fast and scalable octic-equivariant layers.
- (c) We validate our approach through extensive experiments in Section 4 on two representative ViT models (DeiT III and DINOv2), showcasing strong performance gains at scale.

2 Related Work

Vision Transformer. The Vision Transformer (ViT) was introduced by Dosovitskiy et al. [21] and has subsequently achieved state-of-the-art results in many domains of computer vision [10, 39, 31, 22, 50]. Zhai et al. [57] showed that ViTs benefit from scaling up to 2B parameters and Dehghani et al. [17] extended this to 22B parameters. To support scaling, Chen et al. [12] explored sparse ViTs, while techniques from the language domain—such as parallel layers [49]—have been adopted to improve efficiency. Additionally, Alabdulmohsin et al. [1] investigated which architectural dimensions are most effective to scale. In this work, we propose the incorporation of octic layers in ViTs to increase efficiency at scale. Our motivation follows the likes of Swin Transformers [34] and SparseViT [12], making use of inherent properties of images to improve efficiency.

Equivariant Networks. The equivariance of CNNs to (cyclic) image translations can be extended to incorporate larger symmetry groups such as rotations and reflections, as shown by Cohen and Welling [13], Dieleman et al. [20] using Group Equivariant CNNs (G-CNNs). Cohen and Welling [14], Weiler and Cesa [52] generalized G-CNNs to steerable CNNs, where the features transform according to general group representations. Our octic ViTs can be seen as a more scalable ViT analogue of the octic steerable CNNs by Cohen and Welling [14]. There have also been prior efforts on attention- and Transformer-based equivariant vision architectures [41, 56, 33]. Our work is part of an ongoing research direction of studying and improving the scalability of equivariant networks [6, 4, 5, 36, 47]. Prior work in this direction mostly focused on point cloud data, with the notable exception of Bökman et al. [8] who considered images. In particular, Bökman et al. [8] demonstrated that incorporating horizontal mirroring equivariance into modern image classifiers increases compute efficiency while maintaining representational power. Building on this, we extend the symmetry to the octic group and show in more extensive experiments the practical usefulness of equivariance for two popular ViT training objectives.

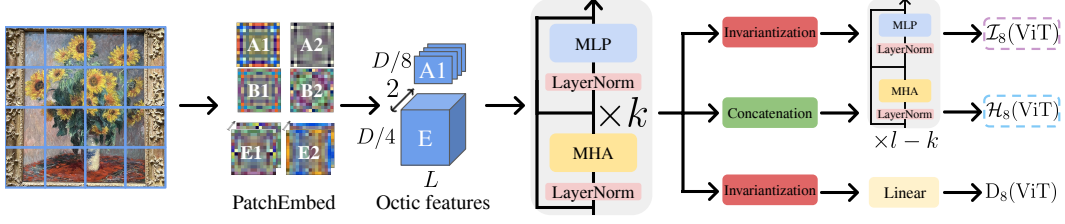


Figure 2: **Architecture.** Patches are first extracted from an image using specialized octic filters and the resulting features are processed by k octic ViT blocks. The final patch embeddings can be fed to $l - k$ standard Transformer blocks (as demonstrated by our \mathcal{H}_8 and \mathcal{I}_8 ViTs) or be used for, e.g., classification by producing an invariant quantity, as in our \mathcal{D}_8 (ViT).

3 Method

Group equivariant networks are networks that respect a data symmetry [55, 13]. For surveys of equivariant networks we refer to [7, 25, 53], and for background on group and representation theory we refer to [44]. In this section, we design octic-equivariant ViT layers.

We begin by preliminaries for octic equivariance in Section 3.1, followed by specifics of the Transformer layers in Section 3.2 and a detailed discussion of computational efficiency in Section 3.3. We summarize the most important notation in Section 3.1.1.

3.1 Preliminaries on Octic Equivariance

In this work we focus on the dihedral group with eight elements, $D_8 = \{e, r, r^2, r^3, s, sr, sr^2, sr^3\}$, such that $r^4 = s^2 = e$ is the identity element and $r^3 = srs$.¹ We think of D_8 as acting on images by reflections s and 90° rotations r , as illustrated in Figure 3. D_8 is also called the octic group, and we opt for this shorter name throughout.

We consider network layers as maps between real group representations of D_8 . In our setting, a real representation is a vector space \mathbb{R}^n equipped with a group homomorphism ρ from D_8 to the group of $n \times n$ invertible real matrices. In other words for every $g \in D_8$, $\rho(g)$ is an invertible matrix and for every $g, h \in D_8$, $\rho(gh) = \rho(g)\rho(h)$. ρ specifies how $x \in \mathbb{R}^n$ transforms under D_8 . A representation of D_8 is also defined by choosing matrices $\rho(r)$ and $\rho(s)$ such that $\rho(r)^4 = \rho(s)^2 = I$ and $\rho(r)^{-1} = \rho(s)\rho(r)\rho(s)$. There are only a few different representations of D_8 used in this work, we list them below as examples. Finally, it is worth mentioning that all representations considered here are orthogonal, i.e., satisfy $\rho(g)^{-1} = \rho(g)^T$.

The atomic building blocks of group representations are the so-called irreducible representations.

Example 3.1 (Irreducible representations). The five irreducible representations, short irreps, of D_8 are defined by

$$\begin{aligned} \rho_{A1}(r) &= \rho_{A1}(s) = 1; & \rho_{A2}(r) &= 1, \rho_{A2}(s) = -1; \\ \rho_{B1}(r) &= -1, \rho_{B1}(s) = 1; & \rho_{B2}(r) &= \rho_{B2}(s) = -1; \\ \text{and } \rho_E(r) &= \begin{pmatrix} 0 & -1 \\ 1 & 0 \end{pmatrix}, \rho_E(s) = \begin{pmatrix} -1 & 0 \\ 0 & 1 \end{pmatrix}. \end{aligned} \quad (1)$$

We use the same notation as the original work on steerable CNNs [14] for these irreps, but choose a different basis for ρ_E . It is known from elementary representation theory that any representation of D_8 can be decomposed into irreps as

$$\rho(g) = Q \left(\bigoplus_{i \in \{A1, A2, B1, B2, E\}} m_i \rho_i(g) \right) Q^{-1} \quad (2)$$

where \bigoplus denotes direct sum of representations, or stacking matrices in a block diagonal, and we write $m_i \rho_i(g)$ for \bigoplus ing $\rho_i(g)$ with itself m_i times. Here Q is an invertible matrix and the m_i are integers specifying the multiplicity of each irrep.

¹The reader is cautioned that D_8 is sometimes alternatively denoted D_4 .

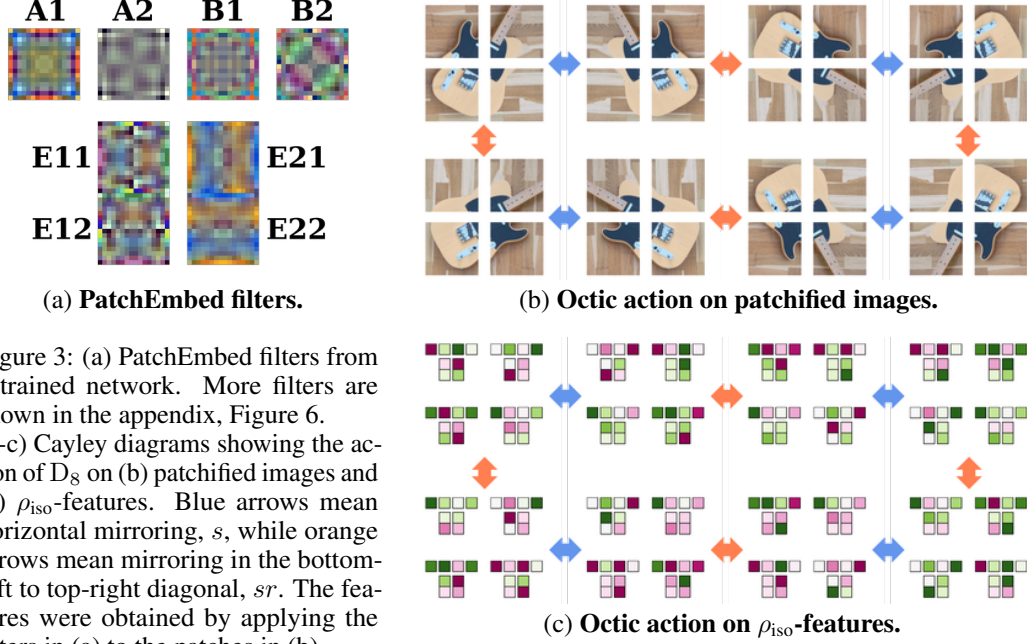


Figure 3: (a) PatchEmbed filters from a trained network. More filters are shown in the appendix, Figure 6. (b-c) Cayley diagrams showing the action of D_8 on (b) patchified images and (c) ρ_{iso} -features. Blue arrows mean horizontal mirroring, s , while orange arrows mean mirroring in the bottom-left to top-right diagonal, sr . The features were obtained by applying the filters in (a) to the patches in (b).

Example 3.2 (Regular representation). The regular representation ρ_{reg} can be thought of as D_8 acting canonically on the vector space of functions $\phi : D_8 \rightarrow \mathbb{R}$:

$$[\rho_{\text{reg}}(g)\phi](h) = \phi(g^{-1}h). \quad (3)$$

We identify each $\phi : D_8 \rightarrow \mathbb{R}$ with the vector

$$(\phi(e) \quad \phi(r^3) \quad \phi(r^2) \quad \phi(r) \quad \phi(s) \quad \phi(sr^3) \quad \phi(sr^2) \quad \phi(sr))^T \in \mathbb{R}^8 \quad (4)$$

so that $\rho_{\text{reg}}(g)$ can be written as a permutation matrix. Importantly, ρ_{reg} commutes with pointwise activation functions such as GELU [27].

Example 3.3 (Isotypical decomposition / Fourier transform). The regular representation ρ_{reg} can be block-diagonalized to its isotypical decomposition ρ_{iso} through (2) as $\rho_{\text{reg}}(g) = Q_{\text{reg}}\rho_{\text{iso}}(g)Q_{\text{reg}}^{-1}$ with

$$\rho_{\text{iso}}(g) = \rho_{A1}(g) \oplus \rho_{A2}(g) \oplus \rho_{B1}(g) \oplus \rho_{B2}(g) \oplus 2\rho_E(g). \quad (5)$$

It is a general fact for finite groups that the regular representation decomposes into all irreps with multiplicities equal to their dimensions. The change of basis Q_{reg} (written out in full in Appendix A) is the inverse Fourier transform of D_8 , with $Q_{\text{reg}}^{-1} = Q_{\text{reg}}^T$ being the Fourier transform.

Equivariant networks use equivariant linear layers, which map between representations. A linear G -equivariant map or intertwiner, $W \in \mathbb{R}^{n \times n}$, between representations ρ_1, ρ_2 , commutes with their action, i.e., $\rho_2(g)W = W\rho_1(g)$. It follows from Schur's lemma that $W = \lambda I$ for some scalar λ if ρ_1, ρ_2 are irreps, and that $\lambda = 0$ if ρ_1, ρ_2 are not isomorphic [44, Section I.2.2]². As ρ_{iso} is just a stack of irreducible representations, any intertwiner between such representations will be sparse, which is why they are less computationally expensive than ordinary linear layers. The naive computational complexity for a linear map $W : \mathbb{R}^{|D_8|} \rightarrow \mathbb{R}^{|D_8|}$ is $|D_8|^2 = 64$ operations. In contrast, intertwiners $\rho_{\text{iso}} \rightarrow \rho_{\text{iso}}$ require a total of $\sum_i m_i^2 d_i = 1 + 1 + 1 + 1 + 2^2 \cdot 2 = 12$ operations for D_8 . From a signal processing perspective, this is analogous to the computational saving of convolution being point-wise multiplications in frequency space.

Example 3.4 (Images). Square images can be considered as elements of $\mathbb{R}^{M \times M \times C}$ where M is the image height/width in pixels and C is the number of colour channels (typically $C = 3$). There

²We can apply Schur's lemma for complex representations here since the irreps listed in Example 3.1 are irreducible over the complex numbers. We will however only use real-valued linear layers, i.e. $\lambda \in \mathbb{R}$.

is a natural D_8 -representation ρ_{image} associated with square images, where $\rho_{\text{image}}(r)$ is the pixel permutation rotating the images anti-clockwise by 90° and $\rho_{\text{image}}(s)$ is the permutation reflecting the images left-to-right.

Example 3.5 (ViT features). In ViTs, features are elements of $\mathbb{R}^{N \times N \times D}$, which we will think of as $N^2 \times D$ matrices. Here, N is the number of image tokens along the height/width of the image, so $N = M/P$ where P is the patch size (typically $P = 14$ or $P = 16$) and D is the channel dimension. The simplest representation that we consider on features is the permutation representation ρ_{token} that, analogously to ρ_{image} , permutes the tokens according to elements of D_8 .

Example 3.6 (Steerable ViT features). We can equip the channel dimension of ViT features with a group representation ρ_{chan} to obtain “steerable” features. If D is divisible by 8, we can consider multiples of ρ_{reg} or ρ_{iso} as ρ_{chan} . The complete representation ρ acting on the $N^2 \times D$ -matrix \mathbf{x} , is then permuting the tokens according to ρ_{token} and modifying the channels according to ρ_{chan} . Concretely,

$$\rho(g)\text{Vec}(\mathbf{x}) = \text{Vec}(\rho_{\text{token}}(g)\mathbf{x}\rho_{\text{chan}}(g)^\top) = (\rho_{\text{chan}}(g) \otimes \rho_{\text{token}}(g)) \text{Vec}(\mathbf{x}), \quad (6)$$

where $\text{Vec}(\mathbf{x})$ is the column-wise vectorization of the matrix \mathbf{x} and \otimes is the tensor product of representations or (equivalently) the Kronecker product of matrices. We refer to features transforming according to (6) as ρ_{chan} -steerable, or features of type ρ_{chan} . This is a simpler form of the induced representations typically considered in steerable CNNs [14, 52], the simplification coming from the fact that we don’t enforce translation equivariance. Steerable ViT-features are illustrated in Figure 3.

Example 3.7 (Patchification of images). One can consider a patchified image as a steerable ViT feature in the following way. By patchification we mean the operation of reshaping an $M \times M \times C$ image first to N^2 patches of size $P \times P$, with $NP = M$ and then to an $N^2 \times (P^2C)$ matrix. When we transform the original image by ρ_{image} , the patchified image is rotated by ρ_{token} and ρ_{chan} as in (6). Now $\rho_{\text{chan}}(g)$ is a permutation matrix that rotates or mirrors a patch and we will denote this particular ρ_{chan} by ρ_{patch} .

We construct ViT versions that map images to steerable ViT features $\mathbf{x} \in \mathbb{R}^{L \times D}$ in the first layer (PatchEmbed) and then process steerable ViT features in subsequent layers. We choose ρ_{chan} to be a multiple of ρ_{iso} , enabling efficient linear layers. Typically, we write $\rho_{\text{chan}} = \frac{D}{8}\rho_{\text{iso}}$ where D is the embedding dimension of the ViT. For classification tasks, we map the steerable ViT features to D_8 invariant features fed into a classification head. We denote ViTs that use ρ_{chan} -steerable features in all layers as $D_8(\text{ViT})$. We will also consider networks that use ρ_{chan} -steerable features for the first layers and then map either to $D\rho_{A1}$ -steerable features, these networks are denoted $\mathcal{I}_8(\text{ViT})$, or break equivariance, denoted $\mathcal{H}_8(\text{ViT})$. We refer to ViTs that fall into these three families broadly as octic ViTs. More details will be given in Section 4.2.

A commonly appreciated fact is that Transformer components b such as MLP and Attention are permutation equivariant over tokens, which implies that

$$b(\rho_{\text{token}}(g)\mathbf{x}) = \rho_{\text{token}}(g)b(\mathbf{x}). \quad (7)$$

For b to be fully equivariant it also needs to be equivariant in the channel dimension

$$b(\rho_{\text{token}}(g)\mathbf{x}\rho_{\text{chan}}(g)^\top) = \rho_{\text{token}}(g)b(\mathbf{x})\rho_{\text{chan}}(g)^\top. \quad (8)$$

In terms of an individual token $x \in \mathbb{R}^D$ transforming according to ρ_{chan} we will write this as

$$b(\rho_{\text{chan}}(g)x) = \rho_{\text{chan}}(g)b(x). \quad (9)$$

Designing the components of octic ViT blocks so that they satisfy (8) is the topic of Section 3.2.

3.1.1 Notation

For the convenience of the reader, we collect the most important notation in the paper in this section. We use the bold letter \mathbf{x} for ViT features, which have shape $L \times D$, where L is the number of tokens and D the channel dimension. Typically, $L = N^2$, where N is the image height/width in tokens. For an individual D -dimensional token we use the letter x which is often acted on by $\rho_{\text{chan}} = \frac{D}{8}\rho_{\text{iso}}$, in which case we can split x into $D/8$ -dimensional sub-tokens $x_{A1}, x_{A2}, x_{B1}, x_{B2}, x_{E11}, x_{E12}, x_{E21}, x_{E22}$, where the first four transform according to the irreps $\rho_{A1}, \rho_{A2}, \rho_{B1}, \rho_{B2}$ respectively while the $2 \times \frac{D}{8}$ -matrices $(x_{E11} \ x_{E12})^\top$ and $(x_{E21} \ x_{E22})^\top$ both transform according to ρ_E .

3.2 Octic Layers

In this section we detail our implementations of D_8 equivariant Transformer layers. Together, these pieces can be combined into a ViT block $b = b_2 \circ b_1$ where

$$b_1(\mathbf{x}) = \mathbf{x} + \text{MHA}(\text{LN}(\mathbf{x})), \quad b_2(\mathbf{x}) = \mathbf{x} + \text{MLP}(\text{LN}(\mathbf{x})). \quad (10)$$

LN is layer normalization, MHA multi-head self-attention and MLP a $D \rightarrow 4D$ linear map, GELU, and $4D \rightarrow D$ linear map. The blocks can subsequently be stacked, as illustrated in Figure 2.

3.2.1 The Patch Embedding Layer

The first layer in a ViT, following [21], is the patch embedding, short PatchEmbed. In our case, it can be viewed as a mapping from steerable features of type ρ_{patch} to steerable features of type $\frac{D}{8}\rho_{\text{iso}}$ where D is the embedding dimension of the ViT. It is implemented as a convolution over the input image with kernel size and stride equal to the patch size P . The convolution kernels are weight sharing constrained to map to features of the different irreps-types in $\frac{D}{8}\rho_{\text{iso}}$, see Figure 3 for an illustration.

Directly after PatchEmbed, we add a learnable positional encoding $\mathbf{e} \in \mathbb{R}^{L \times D}$ to the features. The positional encoding is not constant over tokens, thereby breaking translation equivariance. To be D_8 equivariant \mathbf{e} must satisfy

$$\rho_{\text{token}}(g)\mathbf{x}\rho_{\text{chan}}(g)^T + \mathbf{e} = \rho_{\text{token}}(g)(\mathbf{x} + \mathbf{e})\rho_{\text{chan}}(g)^T \iff \mathbf{e} = \rho_{\text{token}}(g)\mathbf{e}\rho_{\text{chan}}(g)^T. \quad (11)$$

In words, the positional encoding at a specific token position p must be a $\rho_{\text{chan}}(g)$ -transformed version of the positional encoding at the token position that is permuted to p by $\rho_{\text{token}}(g)$.

After adding the positional encoding, we append a learnable class token $[\text{CLS}] \in \mathbb{R}^{1 \times D}$ [19] to the features. To ensure equivariance, we enforce it to be non-zero only in the A1 feature type.

3.2.2 Linear Layers

Linear layers appear in ViTs both in the MLP block and the MHA block. As mentioned in Section 3.1, equivariant linear layers map between irreps of the same type due to Schur’s lemma. This fact was used to construct efficient reflection-equivariant neural networks by Bökman et al. [8]. Here, we use the same approach for octic equivariance.

To re-iterate, for features of type $\rho_{\text{chan}} = \frac{D}{8}\rho_{\text{iso}}$ we consider each token $x \in \mathbb{R}^D$ split into $x_{A1}, x_{A2}, x_{B1}, x_{B2}, x_E$ of dimensions $D/8, D/8, D/8, D/8$ and $2 \times D/4$. Linear layers map each irrep type to itself, meaning that they are parameterised by four $D/8 \times D/8$ matrices and one $D/4 \times D/4$ matrix, yielding a factor 8 fewer parameters than a general linear layer.

In terms of FLOPs needed to compute the linear layer, $x_i \mapsto x_i W_i$ requires $D/8 \cdot D/8 = D^2/64$ FLOPs for $i \in \{A1, A2, B1, B2\}$ while due to the “weight-sharing” over the two dimensions in ρ_E , it requires $2 \cdot D/4 \cdot D/4 = D^2/8$ FLOPs for $i = E$. In total we therefore get $16/3 \approx 5.33$ times fewer FLOPs than the D^2 required for an ordinary linear layer.

3.2.3 Activation Functions, Layer Norm, Attention and Invariantization

A pointwise activation function σ can be applied equivariantly after transforming the features from the Fourier domain (multiples of ρ_{iso}), to the spatial domain (multiples of ρ_{reg}), as discussed in Example 3.3. In the spatial domain σ can be applied point-wise as this commutes with the permutation representation ρ_{reg} . In our ViTs, following prior work, we apply the GELU [27] activation function.

We implement (token-wise) equivariant layer normalization by transforming each irrep separately to mean 0 followed by division by the total norm over all the irreps.

If two tokens q and k transform according to the same orthogonal representation ρ_{chan} , then $q^T k$ is invariant under D_8 since $(\rho_{\text{chan}}(g)q)^T(\rho_{\text{chan}}(g)k) = q^T \rho_{\text{chan}}(g)^T \rho_{\text{chan}}(g)k = q^T k$. This means that the computation of attention logits in ordinary scaled dot-product attention is invariant, so the subsequent weighted sum over value tokens is equivariant.

To output D_8 invariant classification predictions, we map from features of type $\frac{D}{8}\rho_{\text{iso}}$ to features of type $D\rho_{A1}$ and then use global average pooling over tokens. We ablate different invariantizations to A1-tokens in Appendix C, including linear invariants, triple correlation [43, 29], max filtering [9],

Table 1: **Compute scaling.** We measure the scaling of octic ViTs. The model sizes are taken from Dehghani et al. [17] and we do not train the largest models as part of this work. The numbers ending in “x” describe the improvement over standard ViT statistics of the corresponding octic ViTs.

Model	Width	Depth	MLP	Heads	throughput	FLOPs	Peak Mem.
ViT-L	1024	24	4096	16	1.33x	4.58x	2.44x
ViT-H	1280	32	5120	16	1.57x	4.58x	2.88x
ViT-G	1664	48	8192	16	1.91x	4.88x	4.36x
ViT-e	1792	56	15360	16	2.37x	5.01x	5.30x
ViT-22B	6144	36	24576	48	3.54x	5.18x	5.80x

generators of the ring of invariant polynomials and canonisation of the signal [28]. We find that a power spectrum invariantization works well and settle on that for the remainder of the experiments.

3.3 Computational Efficiency

As Transformers scale, the linear layers dominate the execution time [30]. Thus, as ViTs grow, the FLOPs savings will approach those of the linear layer, a reduction of 5.33 times. We plot the FLOPs savings of a ViT block as the embedding dimension increases in Figure 4a. The computational benefits of octic ViTs are more pronounced at scale, and we benchmark the throughput of various ViT sizes from the literature and their octic counterparts in Table 1.

As shown in Table 1, savings in FLOPs do not translate one-to-one to improvements in throughput (images per second) in our current implementation. However, it is still the case that the throughput is greatly improved. Our models are pure PyTorch with `torch.compile`, except for the GELU nonlinearity. We implement a custom Triton [45] kernel that fuses the GELU nonlinearity with the Fourier and inverse Fourier transforms, limiting memory transfers and kernel invocation overhead. While ordinary GELU is pointwise, the new fused Triton kernel is eight points to eight points. For extra efficiency we implement the Fourier transforms by a FFT on D_8 , described in Appendix A.

Finally, we study the arithmetic intensity of our octic linear layer. The arithmetic intensity measures FLOPs per transferred byte and can be compared with the FLOPs per bandwidth of a given device to obtain a bound on the maximum achievable throughput [2]. The arithmetic intensities are $\frac{2BDF}{P(BD+DF+BF)}$ and $\frac{2BDF/5.33}{P(BD+DF/8+BF)}$ for the standard and octic linear layers, respectively, where B is the batch size in tokens, D is the input dimension, F is the output dimension and P is the precision in bytes. This means that the octic and ordinary layers scale differently. At high scale, not only FLOPs are improved by octic layers but also arithmetic intensity. For instance, for $B = 196$ (one image worth of tokens), $P = 2$ and $F = 4D$ (a typical MLP expansion factor) one can calculate that ordinary linear layers have higher arithmetic intensity up to $D \approx 3200$, whereas octic linear layers have higher arithmetic intensity at larger dimensions. For the experiments in this paper, we are not able to scale to such large dimensions, but still get throughput benefits due to savings in FLOPs, as shown in Table 1.

4 Experiments

In this section, we begin with an ablation study of the number of octic blocks followed by an empirical evaluation of our octic ViTs on both supervised (DeiT III) and self-supervised (DINOv2) tasks. We will release code and weights on GitHub.

4.1 Training algorithms and data

DeiT III [46] (Data Efficient Image Transformers) is a popular and highly tuned supervised training recipe for classification with ViTs on ImageNet. We follow the official implementation.

DINOv2 [37] is a state-of-the-art self-supervised method to extract visual features. It combines iBOT [60] and DINO [11] objectives at scale. We follow the official implementation.

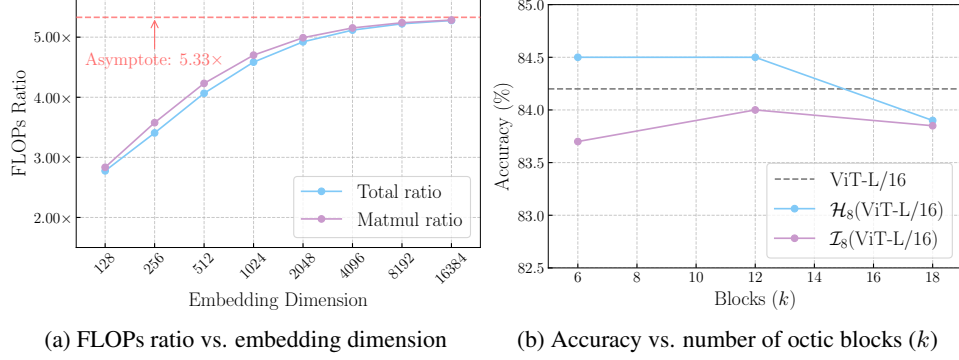


Figure 4: (a) Reduction in FLOPs from a non-equivariant Transformer block to an octic-equivariant block vs. embedding dimension. The matmul ratio reflects only matrix multiplications in linear layers and Attention; the total ratio includes all computations. (b) The effect of changing the number of octic blocks (k) for ViT-L, out of $l = 24$ total blocks.

All of our models are trained on ImageNet-1K [18, 42, 40] with recipes that match the original implementations. In Appendix D, we provide further details on the experiments.

4.2 Ablation of number of octic blocks

We experiment with incorporating non-equivariant blocks [52, 8]. We include networks where the first k of the ViT blocks are octic and the remaining $l - k$ are standard blocks. When we break equivariance in the transition from the equivariant to standard blocks we call the network hybrid (denoted \mathcal{H}_p) and when we map to $D\rho_{A1}$ -steerable features in the transition we refer to the network as early invariant (denoted \mathcal{I}_p). We denote networks with only equivariant layers (mapping to invariant features after the last layer) by \mathcal{D}_p , where p refers to order of the dihedral group. Figure 4b ablates different values of k for ViT-L ($l = 24$). We find that $k = \frac{l}{2}$ strikes a good balance between computational efficiency and representational power and use that for the remainder of the experiments. Note that \mathcal{I}_8 performs worse for small k .

4.3 DeiT III

We train an array of networks on the supervised task of image classification and compare to the performance reported by Touvron et al. [46] and Bökman et al. [8]. We find, as illustrated in Table 2, that incorporating octic-equivariant layers provides significant computational savings while maintaining or improving representational power. In particular, our $\mathcal{H}_8(\text{ViT-H/14})$ model achieves a classification performance of 85.0% compared to the baseline of 84.6% while using only 61% of the FLOPs and matching the performance of the $\mathcal{H}_2(\text{ViT-H/14})$ that incorporates flopping (\mathcal{D}_2) equivariance while being more computational efficient. Similar computational gains are achieved by the invariant model $\mathcal{I}_8(\text{ViT-H/14})$, which achieves a classification performance of 84.7%.

In the final column of Table 2, we study the effect of evaluating models on a randomly rotated validation set without training on such augmentations. We find that the invariant model performs equally well while the performance of the remaining models (including \mathcal{H}_8) significantly degrade.

4.4 DINOv2

As another pretraining task, we consider the DINOv2 recipe and train our own baselines. Results are summarized in Table 3. We find that incorporating octic-equivariant layers maintains or improves downstream classification and segmentation performance while saving FLOPs. In particular, our invariant network $\mathcal{I}_8(\text{ViT-H/16})$ matches the downstream performance of the baseline while using only 61% of the FLOPs and $\mathcal{H}_8(\text{ViT-H/16})$ slightly improves performance with similar savings.

In Appendix D.3, we further investigate the performance of our invariant model and evaluate it on white blood cell classification, a task that lacks a canonical orientation. The invariant model $\mathcal{I}_8(\text{ViT-L/16})$ outperforms the baseline on most evaluated metrics.

Table 2: **DeiT III evaluation.** We measure the Top-1 classification accuracy on ImageNet-1K for different model sizes. We further highlight the computational complexity of each model.

Model	params ($\times 10^6$)	throughput (im/s)	FLOPs ($\times 10^9$)	Peak Mem. (MB)	Top-1 Acc. \uparrow	OOD Rot. Δ Acc. \uparrow
ViT-H/14	632.1	526	167.8	3285	84.6	-12.6
\mathcal{H}_2 (ViT-H/14)	474.2	624	127.4	2734	85.0	N/A
\mathcal{I}_8 (ViT-H/14)	362.3	621	104.0	2249	84.7	0.0
\mathcal{H}_8 (ViT-H/14)	355.8	629	102.3	2223	85.0	-13.4
D ₂ (ViT-H/14)	316.1	734	87.3	2100	84.4	N/A
D ₈ (ViT-H/14)	80.5	830	36.6	1141	82.0	0.0
ViT-L/16	304.4	1317	61.9	1557	84.2	-13.4
\mathcal{H}_2 (ViT-L/16)	228.3	1561	46.9	1458	84.5	N/A
\mathcal{I}_8 (ViT-L/16)	175.5	1511	38.5	1210	84.0	0.0
\mathcal{H}_8 (ViT-L/16)	171.3	1538	37.7	1194	84.5	-13.6
D ₂ (ViT-L/16)	152.2	1753	32.2	1173	83.4	N/A
D ₈ (ViT-L/16)	39.2	1760	13.5	689	79.5	0.0

Table 3: **DINOv2 evaluation.** We evaluate the frozen DINOv2 features by classification accuracy on ImageNet-1K (IN1K) and segmentation mIoU on ADE20K [58, 59] and VOC2012 [23].

Model	FLOPs ($\times 10^9$)	IN1K (acc.) \uparrow		ADE20K (mIoU) \uparrow		VOC2012 (mIoU) \uparrow	
		linear	k -NN	linear	k -NN	linear	k -NN
ViT-H/16	127.7	81.7	81.0	34.7	30.6	70.7	60.9
\mathcal{I}_8 (ViT-H/16)	77.7	81.9	80.9	33.9	29.2	70.6	61.2
\mathcal{H}_8 (ViT-H/16)	77.5	82.2	81.4	35.1	31.1	70.8	61.7
ViT-L/16	61.9	80.9	80.5	33.2	28.4	69.1	58.1
\mathcal{I}_8 (ViT-L/16)	38.5	81.2	80.4	32.6	28.0	70.0	59.6
\mathcal{H}_8 (ViT-L/16)	37.7	81.3	80.8	33.6	29.4	69.1	59.5
D ₈ (ViT-L/16)	13.5	72.2	71.0	23.7	17.6	53.2	42.5

5 Limitations

In this work, we limit our scope to an extensive study of the D₈ group and leave larger dihedral groups for future work. We do not perform hyperparameter tuning and instead replicate the baseline training recipes. Furthermore, we do not conduct an extensive ablation study of the share of features per irrep. We aim to explore this in future work.

We do not realize the full throughput potential of our octic layers, as illustrated by lower throughput gains than FLOPs savings. Our results show promise in continuing work in this direction. Due to computational constraints, we do not replicate the full training of state-of-the-art models such as DINOv2 ViT-G/14. We find that the benefits of octic equivariance increase with model size and expect this trend to persist at even larger scales, which we leave to future work to validate.

6 Conclusion

We introduced octic-equivariant ViT layers that, when incorporated, maintain or improve representational power while significantly reducing computational complexity. We validated our proposed architectures by their effectiveness in both supervised and self-supervised learning. In particular, we achieved approximately 40% reduction in FLOPs for ViT-H while consistently improving performance, positioning octic ViTs as a strong addition to the catalog of vision architectures.

References

- [1] Ibrahim M Alabdulmohsin, Xiaohua Zhai, Alexander Kolesnikov, and Lucas Beyer. Getting vit in shape: Scaling laws for compute-optimal model design. In A. Oh, T. Nau-mann, A. Globerson, K. Saenko, M. Hardt, and S. Levine, editors, *Advances in Neu-ral Information Processing Systems*, volume 36, pages 16406–16425. Curran Associates, Inc., 2023. URL https://proceedings.neurips.cc/paper_files/paper/2023/file/3504a4fa45685d668ce92797fbbf1895-Paper-Conference.pdf.
- [2] Jacob Austin, Sholto Douglas, Roy Frostig, Anselm Levskaya, Charlie Chen, Sharad Vikram, Federico Lebron, Peter Choy, Vinay Ramasesh, Albert Webson, and Reiner Pope. How to scale your model. Online, 2025. Retrieved from <https://jax-ml.github.io/scaling-book/>.
- [3] Erik J Bekkers, Maxime W Lafarge, Mitko Veta, Koen AJ Eppenhof, Josien PW Pluim, and Remco Duits. Roto-translation covariant convolutional networks for medical image analysis. In *Medical Image Computing and Computer Assisted Intervention–MICCAI 2018: 21st In-ternational Conference, Granada, Spain, September 16-20, 2018, Proceedings, Part I*, pages 440–448. Springer, 2018.
- [4] Erik J Bekkers, Sharvaree Vadgama, Rob Hesselink, Putri A Van der Linden, and David W. Romero. Fast, expressive $\mathrm{SE}(n)$ equivariant networks through weight-sharing in position-orientation space. In *The Twelfth International Conference on Learning Representa-tions*, 2024. URL <https://openreview.net/forum?id=dPHLbUqGbr>.
- [5] Vivek Bharadwaj, Austin Glover, Aydin Buluc, and James Demmel. An efficient sparse kernel generator for $\mathrm{o}(3)$ -equivariant deep networks. *arXiv preprint arXiv:2501.13986*, 2025.
- [6] Johann Brehmer, Sönke Behrends, Pim de Haan, and Taco Cohen. Does equivariance matter at scale?, 2024. URL <https://arxiv.org/abs/2410.23179>.
- [7] Michael M. Bronstein, Joan Bruna, Taco Cohen, and Petar Veličković. Geometric Deep Learning: Grids, Groups, Graphs, Geodesics, and Gauges. *arXiv:2104.13478 [cs, stat]*, May 2021.
- [8] Georg Bökman, David Nordström, and Fredrik Kahl. Flopping for flops: Leveraging equivari-ance for computational efficiency, 2025. URL <https://arxiv.org/abs/2502.05169>.
- [9] Jameson Cahill, Joseph W Iverson, Dustin G Mixon, and Daniel Packer. Group-invariant max filtering. *Foundations of Computational Mathematics*, pages 1–38, 2024.
- [10] Nicolas Carion, Francisco Massa, Gabriel Synnaeve, Nicolas Usunier, Alexander Kirillov, and Sergey Zagoruyko. End-to-end object detection with transformers. In *Computer Vision – ECCV 2020: 16th European Conference, Glasgow, UK, August 23–28, 2020, Proceedings, Part I*, page 213–229, Berlin, Heidelberg, 2020. Springer-Verlag. ISBN 978-3-030-58451-1. doi: 10.1007/978-3-030-58452-8_13. URL https://doi.org/10.1007/978-3-030-58452-8_13.
- [11] Mathilde Caron, Hugo Touvron, Ishan Misra, Hervé Jegou, Julien Mairal, Piotr Bojanowski, and Armand Joulin. Emerging properties in self-supervised vision transformers. In *2021 IEEE/CVF International Conference on Computer Vision (ICCV)*, pages 9630–9640, 2021. doi: 10.1109/ICCV48922.2021.00951.
- [12] Xuanyao Chen, Zhijian Liu, Haotian Tang, Li Yi, Hang Zhao, and Song Han. Sparsevit: Revisiting activation sparsity for efficient high-resolution vision transformer. In *IEEE/CVF Conference on Computer Vision and Pattern Recognition (CVPR)*, 2023.
- [13] Taco Cohen and Max Welling. Group equivariant convolutional networks. In *ICML*, 2016.
- [14] Taco Cohen and Max Welling. Steerable CNNs. In *ICLR*, 2017.
- [15] Tri Dao. FlashAttention-2: Faster attention with better parallelism and work partitioning. In *International Conference on Learning Representations (ICLR)*, 2024.
- [16] Timothée Darcet, Federico Baldassarre, Maxime Oquab, Julien Mairal, and Piotr Bojanowski. Cluster and predict latent patches for improved masked image modeling, 2025. URL <https://arxiv.org/abs/2502.08769>.

- [17] Mostafa Dehghani, Josip Djolonga, Basil Mustafa, Piotr Padlewski, Jonathan Heek, Justin Gilmer, Andreas Peter Steiner, Mathilde Caron, Robert Geirhos, Ibrahim Alabdulmohsin, Rodolphe Jenatton, Lucas Beyer, Michael Tschannen, Anurag Arnab, Xiao Wang, Carlos Riquelme Ruiz, Matthias Minderer, Joan Puigcerver, Utku Evci, Manoj Kumar, Sjoerd Van Steenkiste, Gamaleldin Fathy Elsayed, Aravindh Mahendran, Fisher Yu, Avital Oliver, Fantine Huot, Jasmijn Bastings, Mark Collier, Alexey A. Gritsenko, Vighnesh Birodkar, Cristina Nader Vasconcelos, Yi Tay, Thomas Mensink, Alexander Kolesnikov, Filip Pavetic, Dustin Tran, Thomas Kipf, Mario Lucic, Xiaohua Zhai, Daniel Keysers, Jeremiah J. Harmsen, and Neil Houlsby. Scaling vision transformers to 22 billion parameters. In Andreas Krause, Emma Brunskill, Kyunghyun Cho, Barbara Engelhardt, Sivan Sabato, and Jonathan Scarlett, editors, *Proceedings of the 40th International Conference on Machine Learning*, volume 202 of *Proceedings of Machine Learning Research*, pages 7480–7512. PMLR, 23–29 Jul 2023. URL <https://proceedings.mlr.press/v202/dehghani23a.html>.
- [18] Jia Deng, Wei Dong, Richard Socher, Li-Jia Li, Kai Li, and Li Fei-Fei. Imagenet: A large-scale hierarchical image database. In *2009 IEEE Conference on Computer Vision and Pattern Recognition*, pages 248–255, 2009. doi: 10.1109/CVPR.2009.5206848.
- [19] Jacob Devlin, Ming-Wei Chang, Kenton Lee, and Kristina Toutanova. BERT: Pre-training of deep bidirectional transformers for language understanding. In Jill Burstein, Christy Doran, and Tamar Solorio, editors, *Proceedings of the 2019 Conference of the North American Chapter of the Association for Computational Linguistics: Human Language Technologies, Volume 1 (Long and Short Papers)*, pages 4171–4186, Minneapolis, Minnesota, June 2019. Association for Computational Linguistics. doi: 10.18653/v1/N19-1423. URL <https://aclanthology.org/N19-1423/>.
- [20] Sander Dieleman, Jeffrey De Fauw, and Koray Kavukcuoglu. Exploiting cyclic symmetry in convolutional neural networks. In *International conference on machine learning*, pages 1889–1898. PMLR, 2016.
- [21] Alexey Dosovitskiy, Lucas Beyer, Alexander Kolesnikov, Dirk Weissenborn, Xiaohua Zhai, Thomas Unterthiner, Mostafa Dehghani, Matthias Minderer, Georg Heigold, Sylvain Gelly, Jakob Uszkoreit, and Neil Houlsby. An image is worth 16x16 words: Transformers for image recognition at scale. In *International Conference on Learning Representations*, 2021.
- [22] Johan Edstedt, Qiyu Sun, Georg Bökman, Mårten Wadenbäck, and Michael Felsberg. RoMa: Robust Dense Feature Matching. *IEEE Conference on Computer Vision and Pattern Recognition*, 2024.
- [23] Mark Everingham, Luc Van Gool, Christopher Williams, John Winn, and Andrew Zisserman. The pascal visual object classes (voc) challenge. *International Journal of Computer Vision*, 88: 303–338, 06 2010. doi: 10.1007/s11263-009-0275-4.
- [24] Luigi Ferraro, Federico Galetto, Francesca Gandini, Hang Huang, Matthew Mastroeni, and Xianglong Ni. The invariantring package for macaulay2. *Journal of Software for Algebra and Geometry*, 14(1):5–11, 2024.
- [25] Jan E. Gerken, Jimmy Aronsson, Oscar Carlsson, Hampus Linander, Fredrik Ohlsson, Christoffer Petersson, and Daniel Persson. Geometric deep learning and equivariant neural networks. *Artificial Intelligence Review*, 56(12):14605–14662, December 2023. ISSN 1573-7462. doi: 10.1007/s10462-023-10502-7. URL <https://doi.org/10.1007/s10462-023-10502-7>.
- [26] Daniel R. Grayson and Michael E. Stillman. Macaulay2, a software system for research in algebraic geometry. Available at <http://www2.macaulay2.com>.
- [27] Dan Hendrycks and Kevin Gimpel. Gaussian error linear units (gelus). *arXiv preprint arXiv:1606.08415*, 2016.
- [28] Sékou-Oumar Kaba, Arnab Kumar Mondal, Yan Zhang, Yoshua Bengio, and Siamak Ravanbakhsh. Equivariance with learned canonicalization functions. In Andreas Krause, Emma Brunskill, Kyunghyun Cho, Barbara Engelhardt, Sivan Sabato, and Jonathan Scarlett, editors, *Proceedings of the 40th International Conference on Machine Learning*, volume 202 of *Proceedings of Machine Learning Research*, pages 15546–15566. PMLR, 23–29 Jul 2023. URL <https://proceedings.mlr.press/v202/kaba23a.html>.

- [29] Ramakrishna Kakarala. The bispectrum as a source of phase-sensitive invariants for fourier descriptors: a group-theoretic approach. *Journal of Mathematical Imaging and Vision*, 44: 341–353, 2012.
- [30] Jared Kaplan, Sam McCandlish, Tom Henighan, Tom B Brown, Benjamin Chess, Rewon Child, Scott Gray, Alec Radford, Jeffrey Wu, and Dario Amodei. Scaling laws for neural language models. *arXiv preprint arXiv:2001.08361*, 2020.
- [31] Alexander Kirillov, Eric Mintun, Nikhila Ravi, Hanzi Mao, Chloe Rolland, Laura Gustafson, Tete Xiao, Spencer Whitehead, Alexander C. Berg, Wan-Yen Lo, Piotr Dollar, and Ross Girshick. Segment anything. In *Proceedings of the IEEE/CVF International Conference on Computer Vision (ICCV)*, pages 4015–4026, October 2023.
- [32] Valentin Koch, Sophia J Wagner, Salome Kazeminia, Ece Sancar, Matthias Hehr, Julia A Schnabel, Tingying Peng, and Carsten Marr. Dinobloom: a foundation model for generalizable cell embeddings in hematology. In *International Conference on Medical Image Computing and Computer-Assisted Intervention*, pages 520–530. Springer, 2024.
- [33] Soumyabrata Kundu and Risi Kondor. Steerable transformers, 2024. URL <https://arxiv.org/abs/2405.15932>.
- [34] Ze Liu, Yutong Lin, Yue Cao, Han Hu, Yixuan Wei, Zheng Zhang, Stephen Lin, and Baining Guo. Swin transformer: Hierarchical vision transformer using shifted windows. In *2021 IEEE/CVF International Conference on Computer Vision (ICCV)*, pages 9992–10002, 2021. doi: 10.1109/ICCV48922.2021.00986.
- [35] Christian Matek, Sebastian Krappe, Christian Münzenmayer, Torsten Haferlach, and Carsten Marr. An expert-annotated dataset of bone marrow cytology in hematologic malignancies. Data set, 2021. URL <https://doi.org/10.7937/TCIA.AXH3-T579>.
- [36] NVIDIA. cuEquivariance: High-performance equivariant neural networks. URL <https://docs.nvidia.com/cuda/cuequivariance/index.html>.
- [37] Maxime Oquab, Timothée Darcet, Théo Moutakanni, Huy V. Vo, Marc Szafraniec, Vasil Khalidov, Pierre Fernandez, Daniel HAZIZA, Francisco Massa, Alaaeldin El-Nouby, Mido Assran, Nicolas Ballas, Wojciech Galuba, Russell Howes, Po-Yao Huang, Shang-Wen Li, Ishan Misra, Michael Rabbat, Vasu Sharma, Gabriel Synnaeve, Hu Xu, Herve Jegou, Julien Mairal, Patrick Labatut, Armand Joulin, and Piotr Bojanowski. DINOv2: Learning robust visual features without supervision. *Transactions on Machine Learning Research*, 2024. ISSN 2835-8856. URL <https://openreview.net/forum?id=a68SUt6zFt>. Featured Certification.
- [38] Adam Paszke, Sam Gross, Francisco Massa, Adam Lerer, James Bradbury, Gregory Chanan, Trevor Killeen, Zeming Lin, Natalia Gimelshein, Luca Antiga, Alban Desmaison, Andreas Kopf, Edward Yang, Zachary DeVito, Martin Raison, Alykhan Tejani, Sasank Chilamkurthy, Benoit Steiner, Lu Fang, Junjie Bai, and Soumith Chintala. Pytorch: An imperative style, high-performance deep learning library. In H. Wallach, H. Larochelle, A. Beygelzimer, F. d'Alché-Buc, E. Fox, and R. Garnett, editors, *Advances in Neural Information Processing Systems 32*, pages 8024–8035. Curran Associates, Inc., 2019.
- [39] Alec Radford, Jong Wook Kim, Chris Hallacy, Aditya Ramesh, Gabriel Goh, Sandhini Agarwal, Girish Sastry, Amanda Askell, Pamela Mishkin, Jack Clark, Gretchen Krueger, and Ilya Sutskever. Learning transferable visual models from natural language supervision. In *International Conference on Machine Learning*, 2021. URL <https://api.semanticscholar.org/CorpusID:231591445>.
- [40] Benjamin Recht, Rebecca Roelofs, Ludwig Schmidt, and Vaishaal Shankar. Do ImageNet classifiers generalize to ImageNet? In Kamalika Chaudhuri and Ruslan Salakhutdinov, editors, *Proceedings of the 36th International Conference on Machine Learning*, volume 97 of *Proceedings of Machine Learning Research*, pages 5389–5400. PMLR, 09–15 Jun 2019. URL <https://proceedings.mlr.press/v97/recht19a.html>.
- [41] David Romero, Erik Bekkers, Jakub Tomczak, and Mark Hoogendoorn. Attentive group equivariant convolutional networks. In *International Conference on Machine Learning*, pages 8188–8199. PMLR, 2020.

- [42] Olga Russakovsky, Jia Deng, Hao Su, Jonathan Krause, Sanjeev Satheesh, Sean Ma, Zhiheng Huang, Andrej Karpathy, Aditya Khosla, Michael Bernstein, et al. Imagenet large scale visual recognition challenge. *International journal of computer vision*, 115:211–252, 2015.
- [43] Sophia Sanborn and Nina Miolane. A general framework for robust g-invariance in g-equivariant networks. *Advances in Neural Information Processing Systems*, 36:67103–67124, 2023.
- [44] Jean-Pierre Serre. *Linear Representations of Finite Groups*, volume 42 of *Graduate Texts in Mathematics*. Springer, New York, NY, 1977. ISBN 978-1-4684-9460-0 978-1-4684-9458-7. doi: 10.1007/978-1-4684-9458-7. URL <http://link.springer.com/10.1007/978-1-4684-9458-7>.
- [45] Philippe Tillet, H. T. Kung, and David Cox. Triton: an intermediate language and compiler for tiled neural network computations. In *Proceedings of the 3rd ACM SIGPLAN International Workshop on Machine Learning and Programming Languages*, MAPL 2019, page 10–19, New York, NY, USA, 2019. Association for Computing Machinery. ISBN 9781450367196. doi: 10.1145/3315508.3329973. URL <https://doi.org/10.1145/3315508.3329973>.
- [46] Hugo Touvron, Matthieu Cord, and Hervé Jégou. Deit iii: Revenge of the vit. In Shai Avidan, Gabriel Brostow, Moustapha Cissé, Giovanni Maria Farinella, and Tal Hassner, editors, *Computer Vision – ECCV 2022*, pages 516–533, Cham, 2022. Springer Nature Switzerland. ISBN 978-3-031-20053-3.
- [47] Sharvaree Vadgama, Mohammad Mohaiminul Islam, Domas Buracus, Christian Shewmake, and Erik Bekkers. On the utility of equivariance and symmetry breaking in deep learning architectures on point clouds. *arXiv preprint arXiv:2501.01999*, 2025.
- [48] Ashish Vaswani, Noam Shazeer, Niki Parmar, Jakob Uszkoreit, Llion Jones, Aidan N Gomez, Łukasz Kaiser, and Illia Polosukhin. Attention is all you need. In I. Guyon, U. Von Luxburg, S. Bengio, H. Wallach, R. Fergus, S. Vishwanathan, and R. Garnett, editors, *Advances in Neural Information Processing Systems*, volume 30. Curran Associates, Inc., 2017. URL https://proceedings.neurips.cc/paper_files/paper/2017/file/3f5ee243547dee91fbd053c1c4a845aa-Paper.pdf.
- [49] Ben Wang. Mesh-Transformer-JAX: Model-Parallel Implementation of Transformer Language Model with JAX. <https://github.com/kingoflolz/mesh-transformer-jax>, May 2021.
- [50] Jianyuan Wang, Minghao Chen, Nikita Karaev, Andrea Vedaldi, Christian Rupprecht, and David Novotny. Vggt: Visual geometry grounded transformer, 2025. URL <https://arxiv.org/abs/2503.11651>.
- [51] Shuzhe Wang, Vincent Leroy, Yohann Cabon, Boris Chidlovskii, and Jerome Revaud. Dust3r: Geometric 3d vision made easy. In *Proceedings of the IEEE/CVF Conference on Computer Vision and Pattern Recognition (CVPR)*, pages 20697–20709, June 2024.
- [52] Maurice Weiler and Gabriele Cesa. General $E(2)$ -equivariant steerable CNNs. In *NeurIPS*, 2019. URL <https://proceedings.neurips.cc/paper/2019/file/45d6637b718d0f24a237069fe41b0db4-Paper.pdf>.
- [53] Maurice Weiler, Patrick Forré, Erik Verlinde, and Max Welling. *Equivariant and Coordinate Independent Convolutional Networks*. 2023.
- [54] Ross Wightman. Pytorch image models. <https://github.com/rwightman/pytorch-image-models>, 2019.
- [55] Jeffrey Wood and John Shawe-Taylor. Representation theory and invariant neural networks. *Discrete Applied Mathematics*, 69(1-2):33–60, August 1996. ISSN 0166218X. doi: 10/c3qmr6.
- [56] Renjun Xu, Kaifan Yang, Ke Liu, and Fengxiang He. $e(2)$ -equivariant vision transformer. In *Uncertainty in Artificial Intelligence*, pages 2356–2366. PMLR, 2023.

- [57] Xiaohua Zhai, Alexander Kolesnikov, Neil Houlsby, and Lucas Beyer. Scaling vision transformers. In *Proceedings of the IEEE/CVF Conference on Computer Vision and Pattern Recognition (CVPR)*, pages 12104–12113, June 2022.
- [58] Bolei Zhou, Hang Zhao, Xavier Puig, Sanja Fidler, Adela Barriuso, and Antonio Torralba. Scene parsing through ade20k dataset. In *Proceedings of the IEEE Conference on Computer Vision and Pattern Recognition*, 2017.
- [59] Bolei Zhou, Hang Zhao, Xavier Puig, Tete Xiao, Sanja Fidler, Adela Barriuso, and Antonio Torralba. Semantic understanding of scenes through the ade20k dataset. *International Journal of Computer Vision*, 127(3):302–321, 2019.
- [60] Jinghao Zhou, Chen Wei, Huiyu Wang, Wei Shen, Cihang Xie, Alan Yuille, and Tao Kong. ibot: Image bert pre-training with online tokenizer. *International Conference on Learning Representations (ICLR)*, 2022.

A Fourier Transform for D_8

The Inverse Fourier Transform, i.e., changing basis from the Isotypical representation ρ_{iso} to the Regular representation ρ_{reg} , can be written in the case of D_8 as

$$Q_{\text{reg}} = \frac{\sqrt{2}}{4} \begin{pmatrix} 1 & 1 & 1 & 1 & 1 & 1 & 1 & -1 \\ 1 & 1 & -1 & -1 & 1 & -1 & -1 & -1 \\ 1 & 1 & 1 & 1 & -1 & -1 & -1 & 1 \\ 1 & 1 & -1 & -1 & -1 & 1 & 1 & 1 \\ 1 & -1 & 1 & -1 & -1 & 1 & -1 & -1 \\ 1 & -1 & -1 & 1 & -1 & -1 & 1 & -1 \\ 1 & -1 & 1 & -1 & 1 & -1 & 1 & 1 \\ 1 & -1 & -1 & 1 & 1 & 1 & -1 & 1 \end{pmatrix}. \quad (12)$$

In practice, we use a fast Triton-compiled implementation of the mapping $x \mapsto Q_{\text{reg}}x$ as shown in Listing 1, and similarly for $x \mapsto Q_{\text{reg}}^T x$.

Listing 1: Python implementation of Q_{reg} .

```

1 import math
2 SQRT2_OVER_4 = math.sqrt(2) / 4
3
4 def isotypical_to_regular(
5     x_A1, x_A2, x_B1, x_B2, x_E11, x_E12, x_E21, x_E22
6 ):
7     a = x_A1 + x_A2
8     b = x_A1 - x_A2
9     c = x_B1 + x_B2
10    d = x_B1 - x_B2
11    e = x_E11 + x_E12
12    f = x_E11 - x_E12
13    g = x_E21 + x_E22
14    h = x_E21 - x_E22
15    apc = a + c
16    amc = a - c
17    bpd = b + d
18    bmd = b - d
19    eph = e + h
20    emh = e - h
21    fpg = f + g
22    fmg = f - g
23    return (
24        SQRT2_OVER_4 * (apc + eph),
25        SQRT2_OVER_4 * (amc + fmg),
26        SQRT2_OVER_4 * (apc - eph),
27        SQRT2_OVER_4 * (amc - fmg),
28        SQRT2_OVER_4 * (bpd - fpg),
29        SQRT2_OVER_4 * (bmd - emh),
30        SQRT2_OVER_4 * (bpd + fpg),
31        SQRT2_OVER_4 * (bmd + emh)
32    )

```

B Visualizations

B.1 Octic Layers

We visualize how the features are transformed in some of the layers in Figure 5. All layers take in $\frac{D}{8}\rho_{\text{iso}}$ features and output features of the same type. For the linear layer, we use five different weight matrices, one for each irrep, and where weights are shared among the two dimensions of the E features. In the Attention layer, we project the features to query, key and values and flatten them along the final dimension. We can then apply standard multi-head self-attention (MHA) using

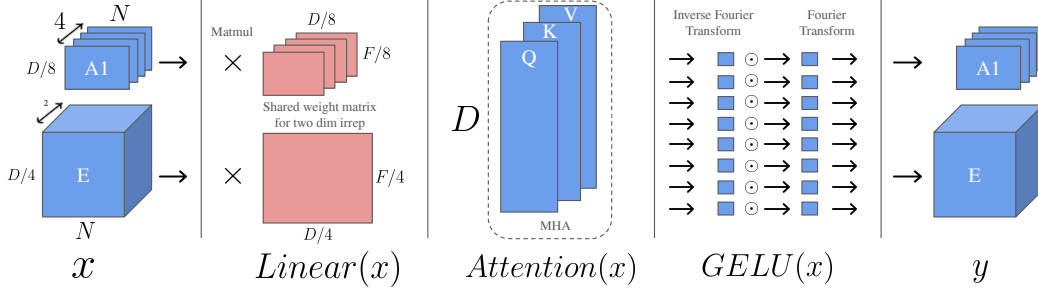


Figure 5: **Octic Layers.** Illustration of how the features are combined in the Linear (left), Attention (middle) and GELU (right) layers.

FlashAttention [15]. Thereafter, we divide the features into the same format as the input to the layer. Non-linearities such as GELU can be applied after transforming the features from ρ_{iso} to ρ_{reg} (through an inverse Fourier transform) and then back to ρ_{iso} .

B.2 Learned Octic Embeddings

The PatchEmbed layer contains filters mapping the input from 3 channel dimensions to D embedding dimensions. To illustrate the learned filters we take inspiration from Dosovitskiy et al. [21] and visualize the first 16 principal components. In contrast to regular ViTs, we have six different learned filters corresponding to the five irreps. Four for the one dimensional and two for the E irrep (due to its multiplicity). The results are illustrated in Figure 6. Interestingly, the learned filters look qualitatively different between the two learning methods. This is similar to how the learned filters of baseline DINOv2 and DeiT III look qualitatively different. DINOv2 training appears to produce more high frequency patterns while DeiT III gives clearer patterns. For the invariant irrep (A1), it appears as though DeiT III training produces a spherical pattern.

C Invariantization

There are multiple options to produce D_8 invariant features, i.e. mapping tokens of type $\rho_{\text{chan}} = \frac{D}{8}\rho_{\text{iso}}$ to features of type $D\rho_{A1}$ (here denoted in short as *invariantization*). We let ψ be a function mapping from features of type $\frac{D}{8}\rho_{\text{iso}}$ to features of type $\frac{KD}{8}\rho_{A1}$ for some K which can be larger or smaller than 8. These $KD/8$ dimensions are then mapped through a small MLP to D dimensions again.

Linear Invariant (Linear). The linear invariant simply extracts the invariant irrep. Here, $K = 1$.

$$\psi(x_{A1}, x_{A2}, x_{B1}, x_{B2}, x_{E11}, x_{E12}, x_{E21}, x_{E22}) = x_{A1}. \quad (13)$$

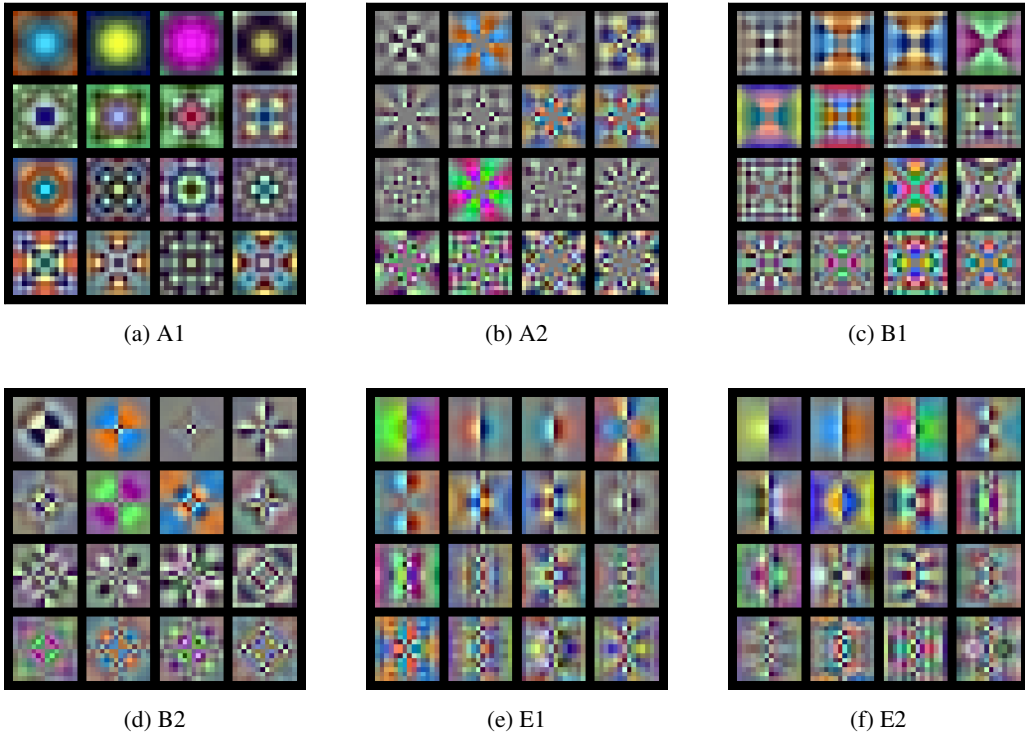
Triple Correlation (Triple Corr.). The triple correlation method [43, 29] extracts a complete set of third order homogeneous polynomial invariants from a signal over D_8 . We computed a basis for all third order invariant homogeneous polynomials using Macaulay2 [26, 24] and use the basis elements as invariant. Here, $K = 15$.

$$\begin{aligned} &\psi(x_{A1}, x_{A2}, x_{B1}, x_{B2}, x_{E11}, x_{E12}, x_{E21}, x_{E22}) \\ &= \left(x_{A1}^3, x_{A1}(x_{E21}^2 + x_{E22}^2), x_{A1}(x_{E11}x_{E21} + x_{E12}x_{E22}), x_{A1}(x_{E11}^2 + x_{E12}^2), x_{A1}x_{B2}^2, x_{A1}x_{B1}^2, x_{A1}x_{A2}^2, \right. \\ &\quad x_{B2}x_{E21}x_{E22}, x_{B2}x_{E12}x_{E21} + x_{B2}x_{E11}x_{E22}, x_{B2}x_{E11}x_{E12}, x_{B1}x_{E21}^2 - x_{B1}x_{E22}^2, \\ &\quad \left. x_{B1}x_{E11}x_{E21} - x_{B1}x_{E12}x_{E22}, x_{B1}x_{E11}^2 - x_{B1}x_{E12}^2, x_{A2}x_{E12}x_{E21} - x_{A2}x_{E11}x_{E22}, x_{A2}x_{B1}x_{B2} \right) \end{aligned} \quad (14)$$

Power spectrum. A common invariant is the power spectrum. We use the following variant, with $K = 6$.

$$\psi(x_{A1}, x_{A2}, x_{B1}, x_{B2}, x_{E1}, x_{E2}) = (x_{A1}, |x_{A2}|, |x_{B1}|, |x_{B2}|, \|x_{E1}\|, \|x_{E2}\|) \quad (15)$$

(a) Octic DeiT III Learned Filters



(b) Octic DINOv2 Learned Filters

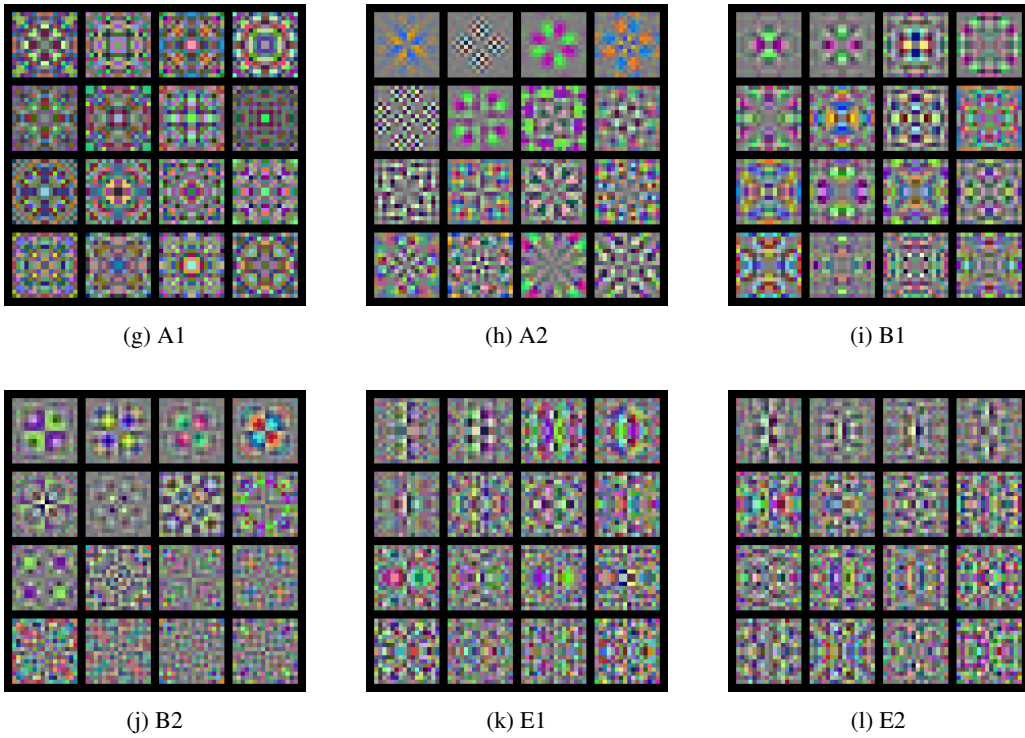


Figure 6: **Comparison of learned patch embedding filters.** (a) DeiT III. (b) DINOv2. Each figure shows the top-16 principal components of the octic PatchEmbed filter for a specific feature type.

Table 4: **Invariantization Ablation.** Comparing classification accuracy using different invariantization methods on ImageNet-1K using the DeiT III training recipe for 400 epochs for D₈ (ViT-L/16).

	Top-1	Top-5
Linear	79.2	94.7
Polynomial	79.4	94.8
Triple Corr.	76.8	93.7
Canonisation	79.5	94.9
Max Filtering	77.9	93.9
Power Spec.	79.5	94.9

Polynomial. Similar to the triple correlation, we can consider a polynomial basis for the full invariant ring. This was computed using Macaulay2, yielding $K = 32$.

$$\begin{aligned}
& \psi(x_{A1}, x_{A2}, x_{B1}, x_{B2}, x_{E11}, x_{E12}, x_{E21}, x_{E22}) \\
&= \left(x_{A1}, x_{E21}^2 + x_{E22}^2, x_{E11}x_{E21} + x_{E12}x_{E22}, x_{E11}^2 + x_{E12}^2, x_{B2}^2, x_{B1}^2, x_{A2}^2, \right. \\
&\quad x_{B2}x_{E21}x_{E22}, x_{B2}x_{E12}x_{E21} + x_{B2}x_{E11}x_{E22}, x_{B2}x_{E11}x_{E12}, x_{B1}x_{E21}^2 - x_{B1}x_{E22}^2, \\
&\quad x_{B1}x_{E11}x_{E21} - x_{B1}x_{E12}x_{E22}, x_{B1}x_{E11}^2 - x_{B1}x_{E12}^2, x_{A2}x_{E12}x_{E21} - x_{A2}x_{E11}x_{E22}, \\
&\quad x_{A2}x_{B1}x_{B2}, x_{E21}^4 + x_{E22}^4, x_{E11}x_{E21}^3 + x_{E12}x_{E22}^3, x_{E11}^2x_{E21}^2 + x_{E12}^2x_{E22}^2, \\
&\quad x_{E11}^3x_{E21} + x_{E12}^3x_{E22}, x_{E11}^4 + x_{E12}^4, \\
&\quad x_{B1}x_{B2}x_{E12}x_{E21} - x_{B1}x_{B2}x_{E11}x_{E22}, x_{A2}x_{B2}x_{E21}^2 - x_{A2}x_{B2}x_{E22}^2, \\
&\quad x_{A2}x_{B2}x_{E11}x_{E21} - x_{A2}x_{B2}x_{E12}x_{E22}, x_{A2}x_{B2}x_{E11}^2 - x_{A2}x_{B2}x_{E12}^2, \\
&\quad x_{A2}x_{B1}x_{E21}x_{E22}, x_{A2}x_{B1}x_{E12}x_{E21} + x_{A2}x_{B1}x_{E11}x_{E22}, x_{A2}x_{B1}x_{E11}x_{E12}, \\
&\quad x_{A2}x_{E21}^3x_{E22} - x_{A2}x_{E21}x_{E22}^3, x_{A2}x_{E12}x_{E21}^3 - x_{A2}x_{E11}x_{E22}^3, \\
&\quad x_{A2}x_{E11}x_{E12}x_{E21}^2 - x_{A2}x_{E11}x_{E12}x_{E22}^2, x_{A2}x_{E11}^2x_{E12}x_{E21} - x_{A2}x_{E11}x_{E12}^2x_{E22}, \\
&\quad \left. x_{A2}x_{E11}^3x_{E12} - x_{A2}x_{E11}x_{E12}^3 \right)
\end{aligned} \tag{16}$$

Max filtering. We follow Cahill et al. [9] and implement a version of their max filtering invariant. For this, we have a set of $2D$ learnable D -dimensional tokens $\mathbf{y} \in \mathbb{R}^{2D \times D}$, and the $2D$ invariants are given by

$$\psi(x) = \bigoplus_{k=1}^{2D} \max_{g \in D_8} \langle \mathbf{y}_k, \rho_{\text{chan}}(g)x \rangle. \tag{17}$$

Canonisation. Similar to the max filtering approach, we implement a canonisation where we have a single learnable D -dimensional reference token y and compute the D -dimensional invariant as

$$\psi(x) = \rho_{\text{chan}} \left(\operatorname{argmax}_{g \in D_8} \langle y, \rho_{\text{chan}}(g)x \rangle \right) x. \tag{18}$$

We conduct a study of the effect of these different invariantization methods. A priori, max filtering and canonisation should be more expressive than the others as they are the only invariants considered here that are able to preserve the relative phase information coming from different phase in different copies of ρ_{iso} . We train D₈(ViT-L/16) on ImageNet-1K following the DeiT III recipe. The results are presented in Table 4. The conclusion is that the simple power spectrum invariant works well, and so we select it as our invariantization of choice in the remainder of the experiments.

D Experimental Setting

D.1 DeiT III

We train for 400 epochs on ImageNet-1K with an effective batch size of 2048 following Touvron et al. [46] and Bökman et al. [8]. We compare to the figures reported in the respective papers

Table 5: **Hyperparameters used in experiments.** Collection of the most important hyperparameters used. For the full set we refer to the original implementations.

(a) DeiT III hyperparameters			(b) DINOv2 hyperparameters		
Model	ViT-L/16	ViT-H/14	Model	ViT-L/16	ViT-H/16
Batch size	128×16	64×32	Batch size	64×16	32×32
Optimizer	LAMB	LAMB	Optimizer	AdamW	AdamW
LR	3×10^{-3}	3×10^{-3}	Base LR	4×10^{-3}	4×10^{-3}
LR decay	cosine	cosine	Init layer scale	1.10^{-5}	1.10^{-5}
Weight decay	0.02	0.02	Weight decay	0.04	0.04
Training epochs	400	400	Training steps	125K	125K
Warmup epochs	5	5	Warmup steps	12.5K	12.5K
Stoch. Depth	0.4	0.5	Drop path	0.3	0.3
Repeated Aug	✓	✓	K	65536	65536
Gradient Clip.	1.0	1.0	Gradient Clip.	3.0	3.0
Mixup alpha	0.8	0.8	Init EMA momentum	0.8	0.8
Cutmix alpha	1.0	1.0	Koleo loss weight	0.1	0.1
ColorJitter	0.3	0.3	iBOT sample prob.	0.5	0.5
Loss	BCE	BCE	iBOT mask ratio	0.1-0.5	0.1-0.5

and thus only train the octic ViTs. The training recipe includes heavy data augmentation (e.g. cutmix, mixup and color jitter) and uses the deprecated NVIDIA Apex library. Training is done in mixed precision with the lamb optimizer. The most important hyperparameters are summarized in Table 5a. For more details, we refer to [46, 8] and the official repo used for reproduction <https://github.com/facebookresearch/deit>.

Out of distribution (OOD) rotation evaluation simply adds a random 90 degree rotation to the validation set of IN1K and computes the classification accuracy on the randomly rotated dataset. Note, as the publicly available weights are trained for 800 epochs (whereas we compare to the figures reported for 400 epochs in the original paper), we compute the OOD Δ on these weights.

D.2 DINOv2

We closely follow the implementation in the original paper, only modifying to train in BF16 instead of FP16 for greater stability, and follow the same evaluation protocol for classification. Lacking an official reproduction of the segmentation protocol in DINOv2, we opt for the evaluation protocol created by Darcet et al. [16] for semantic segmentation on ADE20K and VOC2012. In contrast to the original DINOv2 paper, we decide to limit our study to ViT-L and ViT-H, the latter of which was not included in the original paper. We opt for the larger patch size of $P = 16$ for all our DINOv2 models to save computational resources. Note, this is the reason why we report fewer FLOPs for our DINOv2 ViT-H models than their DeiT III counterpart (which use $P = 14$).

We train on ImageNet-1K for 125K steps with an effective batch size of 1024 using the adamw optimizer. We train our own baselines for fair comparison (to obtain checkpoints after only training on IN1K). The training progression of the ViT-L/16 family can be visualized in Figure 7. The most important hyperparameters are summarized in Table 5b. For exact details about the configuration of hyper parameters we refer to the base configs in the DINOv2 repo <https://github.com/facebookresearch/dinov2>.

We do not implement specific hardware efficient layers for DINOv2 training and instead opt for the standard octic layers that are timm compatible. As such, the octic layers do not leverage NestedTensorBlock and training speedups associated with xFormers. This choice does not impact speed on downstream tasks but slightly decreases pre-training speed.

D.3 DinoBloom

We investigate the performance of our invariant model on white blood cell classification. We follow the procedure of DinoBloom [32] and report our results for ViT-L in Table 7. We find that the invariant model $\mathcal{I}_8(\text{ViT-L}/16)$ outperforms the baseline on most evaluated metrics. We tried evaluating on a rotated test set and found negligible change in performance for the baseline (the invariant model inherently has no change in performance, similar to the last column of Table 2).

For the details of the experiment, we closely follow the training and evaluation protocol of Koch et al. [32]. In particular, we finetune our DINOv2 checkpoints for 4K iterations (taking approx. 1 hour on 8 A100-40GB) and evaluate on a hold-out split of the Bone Marrow Cytomorphology (BMC) [35] dataset. However, we limit our finetuning datasets to the datasets presented in Table 6. Note, we follow the same datasplit of BMC as in DinoBloom and thus also refrain from training on that part.

Table 6: **Hematology datasets.** Dataset mixture for DinoBloom finetuning.

Datasets	Modality	Images
BMC	Bone Marrow	171K
AML Hehr	Blood	102K
APL	Blood	26K
AML Matek	Blood	18K
Acevedo	Blood	17K
Raabing WBC	Blood	10K
Total		354k

D.4 General Settings

Software versioning. We utilize the PyTorch [38] and the timm [54] libraries for our experiments. We run the same versioning as our benchmarks. For all other experiments, we use Python 3.11.9 and PyTorch 2.6.0 with CUDA 11.8.

Model sizes. The model sizes referred to in the paper adhere to the standard terminology used by Wightman [54], Dosovitskiy et al. [21]. If we denote the shape by a tuple of (depth, width, attention heads), ViT-L has shape (24, 1024, 16) and ViT-H has shape (32, 1280, 16). Both use MLP dimension four times the size of the embedding dimension (commonly referred to as MLP ratio).

Calculating throughput. Throughput and peak memory are measured on a single A100-80GB GPU with batch size fixed to 64 using `torch.compile`, FlashAttention [15], and mixed precision. The throughput only measures forward passes with no gradients. Moreover, we utilize 10 warm-up iterations and then average over 100 runs [8]. Peak memory is measured with PyTorch’s device memory allocation monitor.

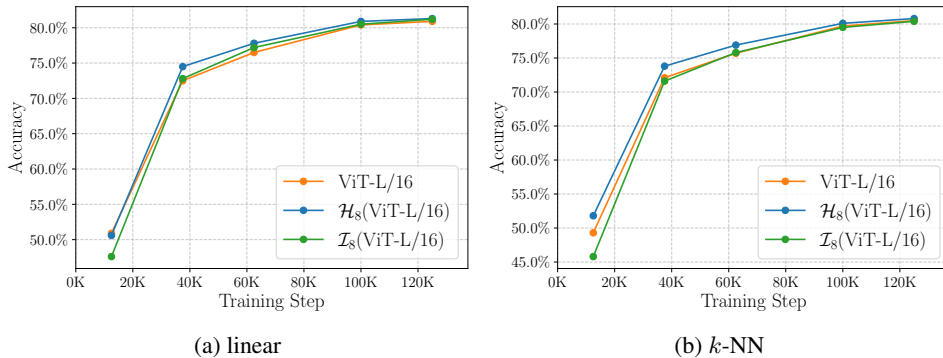


Figure 7: **DINOv2 training progression.** Classification accuracy development during 125K training steps for linear probe and k -NN on frozen features for ViT-L sized models.

Table 7: **Hematology finetuning.** White blood cell classification performance on BMC dataset with 21 highly imbalanced classes after finetuning on hematology data following DinoBloom.

Model	1- k -NN			20- k -NN			Lin. probe		
	wF1	Acc	bAcc	wF1	Acc	bAcc	wF1	Acc	bAcc
ViT-L/16	78.0	78.0	57.6	83.1	83.6	54.9	84.6	84.7	62.2
\mathcal{I}_8 (ViT-L/16)	78.1	78.0	61.3	83.5	83.9	55.7	85.0	85.2	61.9

Counting FLOPs. We count the number of FLOPs using `fvcore.nn.FlopCountAnalysis` <https://github.com/facebookresearch/fvcore>. FLOPs are normalized with respect to the batch size (i.e. we measure FLOPs/image). We acknowledge that the term FLOPs often leads to confusion. We adopt the terminology of prior work [46, 8] and the `fvcore` library for FLOPs, though, strictly speaking, this refers to MACs (as a factor of two is omitted).

D.5 Compute Resources

Table 8 provides information on the computing resources required for the main experiments. The largest single experiment (i.e. not accounting ablation studies) used $32 \times \text{A100-40GB}$ for 58 hours. Failed or discarded results are not included. In total, we used around 20k A100-40GB hours for our main results.

Table 8: **GPU hours.** Exact account of hardware usage for the main experiments. Account does not include failed or discarded experiments or smaller evaluation pipelines such as linear probes and k -NN. Efficiency gains were made progressively and thus some experiments took longer than necessary. Similarly, our training pipeline for DINOv2 is not fully optimized for the octic layers. Resource unit (RU) is measured in A100 equivalent hours where an A40 hour costs 0.54 units.

Experiment	Model	GPUs	Time	RU
DeiT III	\mathcal{I}_8 (ViT-H/14)	$32 \times \text{A100-40GB}$	58h	1856
DeiT III	\mathcal{D}_8 (ViT-H/14)	$32 \times \text{A100-40GB}$	57h	1824
DeiT III	\mathcal{H}_8 (ViT-H/14)	$32 \times \text{A100-40GB}$	55h	1760
DeiT III	\mathcal{H}_8 (ViT-L/16)	$16 \times \text{A100-40GB}$	39h	624
DeiT III	\mathcal{I}_8 (ViT-L/16)	$16 \times \text{A100-40GB}$	37h	592
DeiT III	\mathcal{D}_8 (ViT-L/16)	$16 \times \text{A100-40GB}$	36h	576
Ablation: Invarisation	\mathcal{H}_8 (ViT-L/16)	$16 \times \text{A100-40GB}$	240h	3840
Ablation: Hybridisation	\mathcal{I}_8 (ViT-L/16)	$16 \times \text{A100-40GB}$	122h	1952
Ablation: Hybridisation	\mathcal{H}_8 (ViT-L/16)	$16 \times \text{A100-40GB}$	120h	1920
DINOv2	\mathcal{H}_8 (ViT-H/16)	$32 \times \text{A100-40GB}$	33h	1056
DINOv2	\mathcal{I}_8 (ViT-H/16)	$32 \times \text{A100-40GB}$	30h	960
DINOv2	\mathcal{D}_8 (ViT-L/16)	$32 \times \text{A100-40GB}$	23h	736
DINOv2	ViT-H/16	$32 \times \text{A100-40GB}$	21h	672
DINOv2	\mathcal{I}_8 (ViT-L/16)	$32 \times \text{A100-40GB}$	19h	608
DINOv2	\mathcal{H}_8 (ViT-L/16)	$32 \times \text{A100-40GB}$	19h	608
DINOv2	ViT-L/16	$16 \times \text{A100-40GB}$	24h	384
DinoBloom	\mathcal{I}_8 (ViT-L/16)	$8 \times \text{A100-40GB}$	46min	6
DinoBloom	ViT-L/16	$8 \times \text{A100-40GB}$	37min	5
Total				19979

E Licenses

Data. All our models are trained on ImageNet-1K [18] which has a custom non-commercial license (see <https://www.image-net.org/download.php>). We further evaluate on ADE20K, VOC2012, and BMC. For the licenses see <https://ade20k.csail.mit.edu/terms/>

`index.html`, <http://host.robots.ox.ac.uk/pascal/VOC/voc2012/>, and <https://www.cancerimagingarchive.net/data-usage-policies-and-restrictions/>, respectively.

Images. All the images in this paper are original and taken by the authors. Similarly, illustrations are created by the authors. The assets allow for non-commercial use and redistribution with proper attribution (CC BY-NC).

Code. The efficient octic layers are our original work and will be licensed under Apache License 2.0 following the code release. The training pipelines are from DeiT III [46] and DINOv2 [37] which are both also under the Apache License 2.0. For details about the Apache License 2.0 we refer to <https://www.apache.org/licenses/LICENSE-2.0>.